QUANTIFICATION OF THE INDUCED ELECTRIC FIELD IN A MATERIAL SAMPLE PLACED WITHIN AN ENERGIZED CYLINDRICAL CAVITY

J.-P. Zhang and K.-M. Chen

Department of Electrical and Computer Engineering
Michigan State University
East Lansing, MI 48824, USA

1. INTRODUCTION

The global advantages of microwave processing of material samples over conventional heating have been systematically demonstrated, including fast chemical reaction rate, fast heating rate, and high selectivity. However, the physical mechanism leading to these advantages

for the microwave heating is not well known. To understand this, the interaction of microwave fields and the material samples needs to be investigated. The first task is to study the coupling of the microwave energy into molecules of a material sample. For this study, it is necessary to determine the microwave (EM) energy absorption rate (or dissipated microwave power density) P at any point inside the material sample. To determine P, it is essential to quantify accurately the distribution of the induced electric field at any point inside the material sample. Therefore, the key step to understand the processing of a material sample in an energized electromagnetic cavity is to quantify the induced electric field inside the material sample.

The subject of dielectric-loaded cavities has been studied by a number of workers [1–6] based on the mode-matching method or the surface integral equation method. However, all these studies considered only the cavities loaded with dielectrics which have symmetric geometries. More recent studies on this subject using the finite difference-time domain method, the finite element method or the method of lines have been reported [7–12]. Numerical results of these methods can not provide physical picture of how the microwave modes interact with a material sample.

In this paper, we present a method which solves Maxwell's equations in a cavity in the presence of a material sample based on an Electric Field Integral Equation (EFIE) or a Magnetic Field Integral Equation (MFE). This method is quite powerful because it can deal with a material sample of arbitrary geometry. Also it gives more physical pictures on the coupling of cavity modes with the material sample.

In many studies involving this type of problem, the unknown induced electric field inside the cavity is expanded only in terms of the normal cavity electric modes which are completely solenoidal. This is not correct for the following reason [13–18]. When a material sample is placed in the cavity, the initial cavity electric field will induce electric charges on the surface of the material sample if it is of finite size or at the heterogeneity boundaries if it is heterogeneous. Thus, the divergence of the electric field will not be zero at the locations of the induced charges, or the divergence of the electric field will not vanish at all points in the cavity. Therefore, the normal cavity electric modes which are solenoidal are not sufficient to represent the unknown induced electric field inside the material sample. Additional eigenmodes which are irrotational are needed.

   In this paper, a complete set of vector wave functions which include both solenoidal and irrotational functions are employed and the electric field and magnetic field integral equations are derived based on the expansion of these vector wave functions. When solving the integral equation, the convergence property of the derived dyadic Green's function plays a vital role; thus several methods are explored to increase the convergence rate of the dyadic Green's function. One efficient way to achieve this goal is to reduce the infinite triple summation over the cavity eigenfunctions in the expression of the dyadic Green's function to the infinite double summation. For some material samples with specific geometries, a scheme of separating the material sample into the boundary layer region and the interior volume region is proposed. This scheme tends to improve the convergence of numerical results and also to save computation time.

   Induced electric fields in some material samples with specific geometries have been calculated. Numerical results agree well with some theoretical estimations and analytical results produced by a mode-matching method described in a companion paper [19] in this issue.

2. DERIVATION OF EFIE AND MFIE IN CYLINDRICAL CAVITIES

The eigenfunction expansion of dyadic Green's functions in electromagnetic theory provides a systematic means of constructing and interpreting these dyadics [13]. These functions were first introduced by Hansen [20–22]. In his original work [20], Hansen introduced three kinds of vector wave functions, denoted by $\vec{L}$, $\vec{M}$, and $\vec{N}$, which are the solutions of the homogeneous vector Helmholtz equations. In this paper, three vector wave functions $\vec{L}_{nml}$, $\vec{M}_{nml}$, and $\vec{N}_{nml}$ which are defined in a cylindrical cavity are used as the basis functions to represent the unknown scattered electric field inside the cylindrical cavity containing a material sample. The orthogonality and completeness of the vector wave functions $\vec{L}_{nml}$, $\vec{M}_{nml}$, and $\vec{N}_{nml}$ assure that they form a complete and orthogonal set of basis functions [23]. The details of these vector wave functions are given in Appendix I.

   The distribution of electromagnetic fields at any point in an energized cylindrical cavity with a non-ionic material sample placed inside can be investigated based on Maxwell's equations. The dielectric parameters of the material sample under consideration are permittivity $\varepsilon = \varepsilon' - j\varepsilon''$, permeability μ_0 and conductivity σ. The dimensions
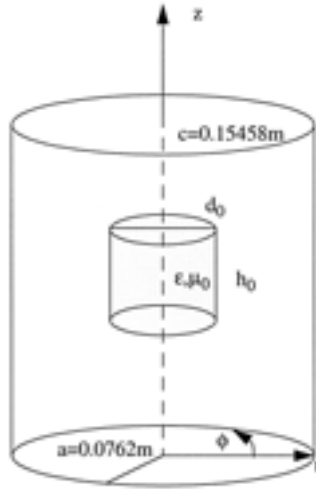
Figure 1. Dimensions of the cylindrical cavity and the material sample. The center of the material sample is consistent with the center of the cavity. The operating frequency is 2.45 GHz.

of the cylindrical cavity and the material sample are shown in Fig. 1. Maxwell's curl equations in the material sample can be written as

$$\begin{cases} \nabla \times \vec{E}(\vec{r}) = -j\omega\mu_0\vec{H}(\vec{r}) \\ \nabla \times \vec{H}(\vec{r}) = \sigma\vec{E}(\vec{r}) + j\omega\varepsilon\vec{E}(\vec{r}) \end{cases} \tag{1}$$

where $\vec{E}(\vec{r})$ and $\vec{H}(\vec{r})$ are the unknown electric and magnetic fields in the material sample we wish to determine. In the empty cavity, the Maxwell's equation is given by

$$\begin{cases} \nabla \times \vec{E}^i(\vec{r}) = -j\omega\mu_0\vec{H}^i(\vec{r}) \\ \nabla \times \vec{H}^i(\vec{r}) = j\omega\varepsilon_0\vec{E}^i(\vec{r}) \end{cases} \tag{2}$$

where $\vec{E}^i(\vec{r})$ and $\vec{H}^i(\vec{r})$ are the initial electric and magnetic fields we assumed.

The initial cavity fields will induce electric currents and charges inside the material sample. These induced electric currents and charges, in turn, will produce the scattered fields or the secondary fields $\vec{E}^s(\vec{r})$ and $\vec{H}^s(\vec{r})$. Thus,

$$\begin{cases} \vec{E}(\vec{r}) = \vec{E}^s(\vec{r}) + \vec{E}^i(\vec{r}) \\ \vec{H}(\vec{r}) = \vec{H}^s(\vec{r}) + \vec{H}^i(\vec{r}) \end{cases} \tag{3}$$

In case the material sample is of finite size or heterogeneous, there will be induced charges on the sample surface or at the heterogeneity boundaries. Thus, $\nabla \cdot \vec{E}^s$ will not be zero at the locations of the induced charges. ($\vec{E}^s(\vec{r})$ has an irrotational component.) However, $\nabla \cdot \vec{H}^s$ is zero at any points inside the cavity even though there is a non-magnetic material sample placed within the cylindrical cavity. The solenoidal eigenfunctions can thus form a complete set of basis functions to represent $\vec{H}^s(\vec{r})$. The wave equations for the scattered fields are derived as

$$\nabla \times \nabla \times \vec{E}^s(\vec{r}) - k_0^2 \vec{E}^s(\vec{r}) = -j\omega\mu_0 \vec{J}_{eq}(\vec{r}) \qquad (4)$$

$$\nabla^2 \vec{H}^s(\vec{r}) + k_0^2 \vec{H}^s(\vec{r}) = -\nabla \times \vec{J}_{eq}(\vec{r}) \qquad (5)$$

where the equivalent current is given by

$$\vec{J}_{eq}(\vec{r}) = [\sigma + j\omega(\varepsilon - \varepsilon_0)]\vec{E}(\vec{r}) = \tau_e(\vec{r})\vec{E}(\vec{r}) \qquad (6)$$

$\tau_e(\vec{r}) = \sigma + j\omega(\varepsilon - \varepsilon_0)$ is the equivalent complex conductivity, and $k_0^2 = \omega^2\mu_0\varepsilon_0$.

Representing the scattered fields in terms of the complete sets of basis functions, we have

$$\vec{E}^s(\vec{r}) = \sum_n \left[a_n \vec{L}_n(\vec{r}) + b_n \vec{M}_n(\vec{r}) + c_n \vec{N}_n(\vec{r}) \right] \qquad (7)$$

$$\vec{H}^s(\vec{r}) = \sum_n d_n \vec{H}_n(\vec{r}) \qquad (8)$$

where $\vec{H}_n(\vec{r})$ is the normal cavity magnetic mode. Substituting Eqs. (7) and (8) into the wave Eqs. (4) and (5), we obtain the expressions for the scattered fields (see details in Appendix II) as

$$\vec{E}^s(\vec{r}) = -j\omega\mu_0 \int_{V_{\text{sample}}} \tau_e(\vec{r}') \vec{E}(\vec{r}') \cdot \overline{G}_{e0}(\vec{r}',\vec{r})\, dv' + \frac{j\omega\mu_0\tau_e(\vec{r})\vec{E}(\vec{r})}{k_0^2} \qquad (9)$$

$$\vec{H}^s(\vec{r}) = \int_{v_{\text{sample}}} \vec{J}_{eq}(\vec{r}') \cdot \overline{G}_m(\vec{r}',\vec{r})\, dv' \qquad (10)$$

where the dyadic Green's functions are given as (see Appendix II and [23]),

$$\overline{G}_{e0}(\vec{r}',\vec{r}) = \sum_n \left[q_n^2 \frac{\vec{M}_n(\vec{r}')\,\vec{M}_n(\vec{r})}{k_0^2\left(q_n^2 - k_0^2\right)} + k_n^2 \frac{\vec{N}_n(\vec{r}')\,\vec{N}_n(\vec{r})}{k_0^2\left(k_n^2 - k_0^2\right)} \right] \qquad (11)$$

$$\overline{G}_m\left(\vec{r}',\vec{r}\right) = -\frac{\mu_0}{\varepsilon_0}\sum_n \frac{\nabla' \times \vec{H}_n\left(\vec{r}'\right)\vec{H}_n(\vec{r})}{p_n^2 - k_0^2} \tag{12}$$

and $q_n^2 = \left(\frac{p'_{nm}}{a}\right)^2 + \left(\frac{l\pi}{c}\right)^2$, $k_n^2 = \left(\frac{p_{nm}}{a}\right)^2 + \left(\frac{l\pi}{c}\right)^2$ are the respective eigenvalues of the basis functions $\vec{M}_n$ and $\vec{N}_n$. In Eq. (12), p_n is equal to either q_n or k_n. Therefore, EFIE and MFIE can be derived from Eqs. (3), (9), and (10) as

$$\vec{E}(\vec{r})\left(1 - \frac{j\omega\mu_0\tau_e(\vec{r})}{k_0^2}\right) + j\omega\mu_0\int\limits_{v_{\text{sample}}}\tau_e\left(\vec{r}'\right)\vec{E}\left(\vec{r}'\right)\cdot\overline{G}_{e0}\left(\vec{r}',\vec{r}\right)dv' = \vec{E}^i(\vec{r}) \tag{13}$$

$$\vec{H}(\vec{r}) - \int\limits_{v_{\text{sample}}}\tau_e\left(\vec{r}'\right)\frac{\nabla' \times \vec{H}\left(\vec{r}'\right)}{\sigma + j\omega\varepsilon}\cdot\overline{G}_m\left(\vec{r}',\vec{r}\right)dv' = \vec{H}^i(\vec{r}) \tag{14}$$

After some mathematical manipulations, EFIE (13) and MFIE (14) can be proved to be consistent [23]. Therefore, we will only solve EFIE (13) in the following sections. It is noted that some details of the derivation of EFIE are given in Appendix II to show that a delta function in the original dyadic Green's function was extracted to reach the EFIE of Eq. (13). This may help in an explanation given in the numerical example of a thin dielectric rod material sample about the extraction of a delta function. The derivation of MFIE is quite lengthy, thus, interested readers are referred to [23].

3. GALERKIN'S METHOD

Pulse functions are used as both basis and testing functions in the moment method. The material sample is divided into M volume cells and $\vec{E}(\vec{r})$ is assumed to be constant in each subvolume cell. We will denote the mth subvolume by v_m and the position of a representative interior point of v_m by $\vec{r}_m$. After some manipulations for EFIE (13) [23], we obtain

$$\sum_{l=1}^{M}\left[\left(1 - \frac{j\omega\mu_0}{k_0^2}\int\limits_{v_n}\tau_e(\vec{r})dv\right)\overline{I}\delta_{nl} + j\omega\mu_0\overline{G}_{ienl}(\vec{r}_l,\vec{r}_n)\right]\cdot\vec{E}(\vec{r}_l)$$
$$= \vec{E}^i(\vec{r}_n)v_n \tag{15}$$

where

$$\overline{G}_{ienl}(\vec{r}_l, \vec{r}_n) = \int\limits_{v_l} \tau_e\left(\vec{r}'\right) \int\limits_{v_n} \overline{G}_{e0}\left(\vec{r}', \vec{r}\right) \, dv \, dv' \qquad (16)$$

$$\delta_{nl} = \begin{cases} 1 & \text{if } n = l \\ 0 & \text{if } n \neq l \end{cases} \qquad (17)$$

I is a unit dyadic and $n = 1, 2, \ldots, M$. Equation (15) can be expressed in a matrix format as

$$[A_{nl}]_{3M \times 3M} \cdot [E_l]_{3M \times 1} = [B_l]_{3M \times 1} \qquad (18)$$

where

$$[A_{nl}]_{3M \times 3M} = \begin{bmatrix} \left[\overline{A}_{nl}\right]_{rr} & \left[\overline{A}_{nl}\right]_{r\varphi} & \left[\overline{A}_{nl}\right]_{rz} \\ \left[\overline{A}_{nl}\right]_{\varphi r} & \left[\overline{A}_{nl}\right]_{\varphi\varphi} & \left[\overline{A}_{nl}\right]_{\varphi z} \\ \left[\overline{A}_{nl}\right]_{zr} & \left[\overline{A}_{nl}\right]_{z\varphi} & \left[\overline{A}_{nl}\right]_{zz} \end{bmatrix} \qquad (19)$$

$$\overline{A}_{nl} = \left(1 - \frac{j\omega\mu_0}{k_0^2} \int\limits_{v_n} \tau_e(\vec{r}) \, dv\right) \overline{I} \delta_{nl} + j\omega\mu_0 \overline{G}_{ienl}(\vec{r}_l, \vec{r}_n) \quad (20)$$

$$[E_l]_{3M \times 1} = [E_{1r} \ldots E_{Mr} \, E_{1\varphi} \ldots E_{M\varphi} \, E_{1z} \ldots E_{Mz}] \qquad (21)$$

$$[B_l]_{3M \times 1} = [E_r^i(\vec{r}_1)v_1 \ldots E_r^i(\vec{r}_M)v_M \, E_\varphi^i(\vec{r}_1)v_1 \ldots E_\varphi^i(\vec{r}_M)v_M$$
$$\cdot E_z^i(\vec{r}_1)v_1 \ldots E_z^i(\vec{r}_M)v_M]^T \qquad (22)$$

4. NUMERICAL TECHNIQUES

In the matrix composition (19), the integrations of the dyadic Green's function $\overline{G}_{eo}(\vec{r}', \vec{r})$ with respect to both variables $\vec{r}$ and $\vec{r}'$ at different points in the material sample as specified in Eqs. (16) and (20) need to be carried out. However, the convergence property of the dyadic Green's function $\overline{G}_{eo}(\vec{r}', \vec{r})$ is very poor [24]. This causes its integration to have a poor convergence property also.

To save computation time we can reduce the triple summation in the dyadic Green's function to a double summation based on the following two relations [23]:

$$\sum_{l=1}^{\infty} \frac{\sin\left(\dfrac{l\pi}{c}z\right)\sin\left(\dfrac{l\pi}{c}z'\right)}{k_n^2 - k_0^2} = \frac{c}{2k_{gnm}\sin(k_{gnm}c)}$$
$$\cdot \sin[k_{gnm}(c - z_b)]\sin(k_{gnm}z_s) \quad (23)$$

$$\sum_{l=0}^{\infty} \frac{\varepsilon_{0l}\cos\left(\dfrac{l\pi}{c}z\right)\cos\left(\dfrac{l\pi}{c}z'\right)}{2(k_n^2 - k_0^2)} = \frac{-c}{2k_{gnm}\sin(k_{gnm}c)}$$
$$\cdot \cos[k_{gnm}(c - z_b)]\cos(k_{gnm}z_s) \quad (24)$$

where

$$\varepsilon_{0l} = \begin{cases} 1 & \text{if } l = 0 \\ 2 & \text{if } l \neq 0 \end{cases} \quad (25)$$

$$k_{gnm} = \sqrt{k_0^2 - k_{n0}^2} \quad (26)$$

$$k_{n0}^2 = \left(\frac{p'_{nm}}{a}\right)^2 \text{ or } \left(\frac{p_{nm}}{a}\right)^2 \quad (27)$$

$$z_b \equiv \text{ the greater of } z \text{ or } z' \quad (28)$$

$$z_s \equiv \text{ the lesser of } z \text{ or } z' \quad (29)$$

It is noted that there is a factor of $\sin(k_{gnm}c)$ in the denominators in Eqs. (23) and (24). When $k_{gnm}c = i\pi$, where i is an integer, there exists a singularity. For this case, we could sum over the index l directly by taking into a account a slight shift in the resonant frequency [23]. This procedure is justified from the experimental observation that when a small material sample is placed into a resonant cavity, its resonant frequency will be slightly shifted. Numerically we found that a frequency shift of up to 10% does not affect the final numerical results significantly [23].

If the initial electric field is tangential to the major part of the material sample surface, we found that more summation terms are needed in the computation of the induced electric field. For such case, we suggest the scheme of separating the material sample into interior volume and boundary layer regions to approximately obtain the numerical results. This is because the divergence of the electric field does not vanish only at the boundary of a homogeneous material sample of finite size where

the induced electric charges reside and the divergence of the electric field still vanishes in the interior of a homogeneous material sample. Therefore, the irrotational part of the basis functions will not be needed in the representation of the scattered electric field in the interior volume region. That is, two different EFIEs can be derived for these two different regions. EFIE (13) can be employed in the boundary layer region and a new EFIE may be derived for the interior volume region as follows.

The scattered electric field in the interior volume region of the material sample may be represented only by the vector wave functions $\vec{M}_{nml}$ and $\vec{N}_{nml}$ as

$$\vec{E}^s(\vec{r}) = \sum_{n=1}^{\infty} \left[e_n \vec{M}_n(\vec{r}) + f_n \vec{N}_n(\vec{r}) \right] \tag{30}$$

Substituting Eq. (30) into Eq. (4) and applying some mathematical manipulations (Appendix II or [23]), EFIE for the induced electric field in the interior volume region can be derived as

$$\vec{E}(\vec{r}) + j\omega\mu_0 \int_v \tau_e(\vec{r}') \, \vec{E}(\vec{r}') \cdot \overline{G}_{es}(\vec{r}', \vec{r}) \, dv' = \vec{E}^i(\vec{r}) \tag{31}$$

where the dyadic Green's function in the interior volume region is identified as

$$\overline{G}_{es}(\vec{r}', \vec{r}) = \sum_n \left[\frac{\vec{M}_n(\vec{r}') \, \vec{M}_n(\vec{r})}{q_n^2 - k_0^2} + \frac{\vec{N}_n(\vec{r}') \, \vec{N}_n(\vec{r})}{k_n^2 - k_0^2} \right] \tag{32}$$

After the material sample is divided into the boundary layer and interior volume regions, EFIE (13) is applied to the former and EFIE (31) latter. These two EFIEs can be combined and solved by the Galerkin method to yield a matrix equation similar to Eq. (18). Numerical results demonstrate that the dyadic Green's function given by Eq. (32) may converge much faster than that in EFIE (13) [23]. Therefore, this scheme tends to improve the convergence of numerical results and also produces better results.

5. NUMERICAL EXAMPLES

In the cylindrical cavity, we deal with the Bessel functions or their derivatives and their numerical integrations in the formation of the matrix (19). These numerical integrations require extensive computation and a super computer may be needed to find the numerical solution of the EFIE for a material sample of arbitrary geometry. However, for some special cases we can simplify the expression of the dyadic Green's function and numerically solve the EFIE in the cylindrical cavity.

We assume that a material sample which is azimuthally symmetrical is placed in the center of a cylindrical cavity. If the initial cavity mode is not a function of variable φ, for example TM_{012}, then due to the symmetry property [24, 27] the scattered electric field induced by this material sample and the total electric field in the cavity will not be functions of variable φ. Therefore, in the numerical computation for this special case, the eigenfunctions with $n = 0$ will be sufficient to represent the unknown electric field. The expression for the dyadic Green's function in the double summation format over indices n and m will be further reduced to the single summation format over index m.

In the following numerical computations, the dimensions of the cylindrical cavity are shown in Fig. 1. The initial cavity mode is TM_{012} and the resonant frequency of the empty cavity operating at this initial mode is 2.45 GHz. This resonant frequency of the cavity will shift slightly downward when a material sample is placed inside as discussed in [23]. A material sample in the form of a circular cylinder with the diameter d_0 and the height h_0 is placed in the center of the cylindrical cavity as shown in Fig. 1. Using the Galerkin method, the material sample is uniformly divided into $M = n_d \times l_d$ volume cells, where n_d and l_d are the numbers of the volume cells in the r and z directions, respectively. Several material samples with selected shapes and dimensions have been studied, and numerical results were compared with some theoretical approximations and analytical results of a mode-matching method.

5.1 Cubic-Like Material Sample

The dimensions of the cubic-like material sample, having the diameter equal to the height, are set to be $d_0 = 0.004\,\mathrm{m}$ and $h_0 = 0.004\,\mathrm{m}$ with $n_d = 1$ and $l_d = 2$. The relative permittivity of the material

sample is $\varepsilon_r = 2.5$. The cavity resonant frequency is assumed to shift down 5% after the material sample is placed inside the cavity. Since the sample is electrically small, the induced electric field inside the material sample can be estimated by the electrostatic field induced inside of a dielectric sphere as $E = \frac{3}{2+\varepsilon_r} E^i$ [24, 27].

Numerical results presented in Figure 2 show that the induced electric fields are uniform in each volume cell and the E_z component of the induced electric field dominates the other two components due to the small dimensions of the material sample. The ratio of the E_z component of the induced electric field to that of the initial electric field in the material sample is found to be 0.65 in each volume cell while the electrostatic estimation of $E_z/E_z^i = \frac{3}{2+\varepsilon_r}$ gives the approximation of 0.667. Thus, numerical results and the theoretical estimation are in satisfactory agreement.

For the stability check of the numerical results, we increase the dimensions of the cubic-like material sample to: $d_0 = 0.02\,\text{m}$ and $h_0 = 0.02\,\text{m}$ with $n_d = 5$ and $l_d = 10$. The numerical results are shown in Fig. 2 where the cavity resonant frequency shift is assumed to be 8% [23] after the placement of the material sample. Since the z component of the induced electric field dominates, only the ratios of the z components of the induced electric field to that of the initial electric field in the material sample are plotted, in Fig. 2, as a function of r, for the lower half of the sample. (Numerical results are symmetrical with respect to the center of the sample.) We observe that due to the increase in the material sample dimensions, the ratios in Fig. 2 are now reduced to about 0.51 to 0.62. This indicates that the induced electric field in a larger sample will be smaller than the value given by the electrostatic estimation. In Fig. 2, analytical results, produced by a mode-matching method presented in a companion paper [19], for the same material sample are plotted for the comparison. The results of the integral equation method and the mode-matching method agree quite well.

5.2 Thin Disk Material Sample

The dimensions of the material sample with the shape of a thin disk, having its height much smaller than its diameter, are assumed to be $h_0 = 0.002\,\text{m}$ and $d_0 = 0.04\,\text{m}$ with $n_d = 10$ and $l_d = 1$. The relative permittivity of the material sample is $\varepsilon_r = 2.5$. The cavity resonant frequency shift is assumed to be 1% after the material
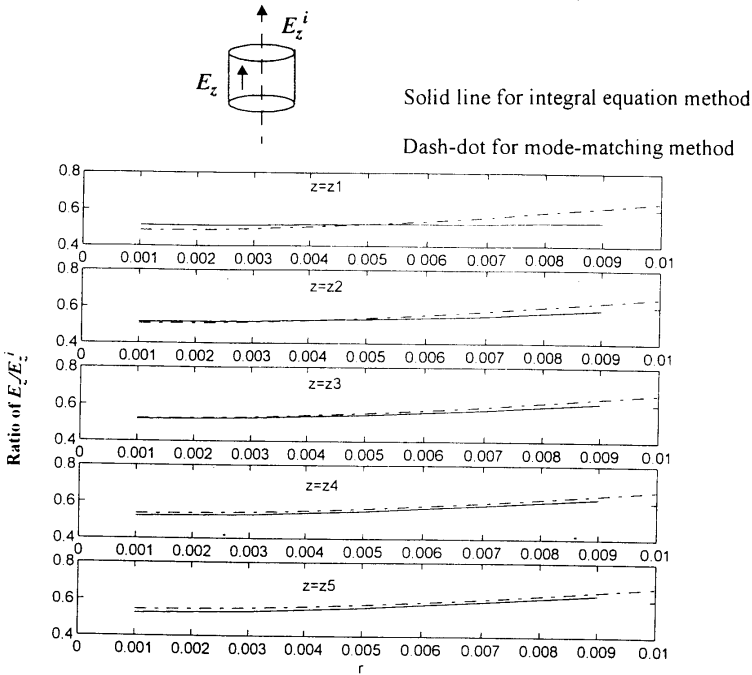
Figure 2. Ratio of E_z/E_z^i varies in the r direction at the different locations of z, obtained from the integral equation method and the mode-matching method. Results of these two different methods are compared to check the numerical accuracy of the former. The dimensions of the material sample are $d_0 = 0.02\,\mathrm{m}$ and $h_0 = 0.02\,\mathrm{m}$ with the relative permittivity of $\varepsilon_r = 2.5$. The initial field is assumed to be a TM_{012} mode operating at $2.45\,\mathrm{GHz}$.

sample is placed inside. Because only the z component of the initial electric field is significant near the center of the cylindrical cavity and the material sample has a thin disk geometry, theoretically the induced electric field in the material sample can be estimated by the boundary condition of $E = (1/\varepsilon_r)E^i = 0.4E^i$. The numerical results are shown in Fig. 3.

In Fig. 3, the ratios of the z component of the induced electric field to that of the initial electric field are plotted as a function of the radial distance, r, of the material sample. We observe that the numerical results are consistent with the theoretical estimation as expected.
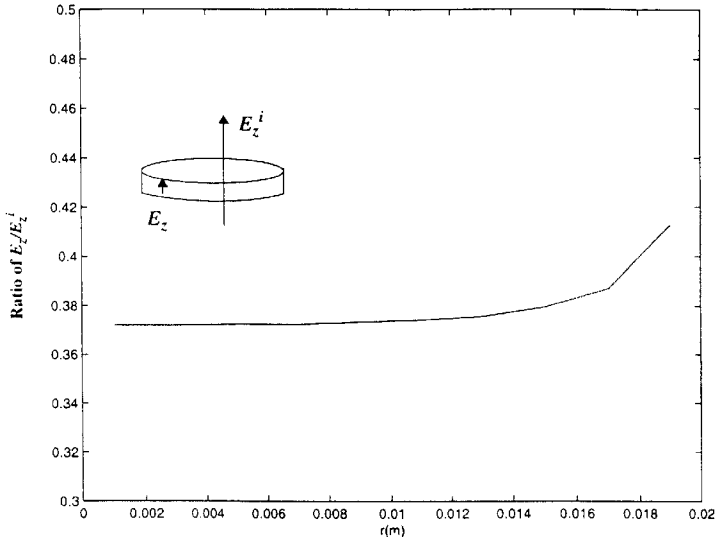
Figure 3. Ratio of E_z/E_z^i varies in the r direction. The dimensions of the material sample are $d_0 = 0.04\,\text{m}$ and $h_0 = 0.002\,\text{m}$ with the relative permittivity of $\varepsilon_r = 2.5$. The initial field is assumed to be a TM_{012} mode operating at $2.45\,\text{GHz}$.

5.3 Thin Dielectric Rod Material Sample

The dimensions of the material sample are: $h_0 = 0.044\,\text{m}$ and $d_0 = 0.008\,\text{m}$ with $n_d = 2$ and $l_d = 22$. The relative permittivity of the material sample is $\varepsilon_r = 2.5$. The cavity resonant frequency shift is assumed to be 1% after the material sample is placed inside. For this case, the induced electric field inside the material sample should be approximately equal to the initial electric field because the initial electric field is tangential to the major part of the material sample surface, and the continuity of the tangential component of the electric field at the material sample surface requires this estimation. The numerical results are shown in Fig. 4.

In Fig. 4, we observe that the maximum ratio of the z-component of the induced electric field to that of the initial electric field is around 0.8 which is not very close to 1. For this ratio to be close to 1 or $\vec{E}(\vec{r}) \approx \vec{E}^i(\vec{r})$, the second term and the third term (the integral) of EFIE (13) should nearly cancel each other. Since the second term was created from the extraction of a delta function from the original
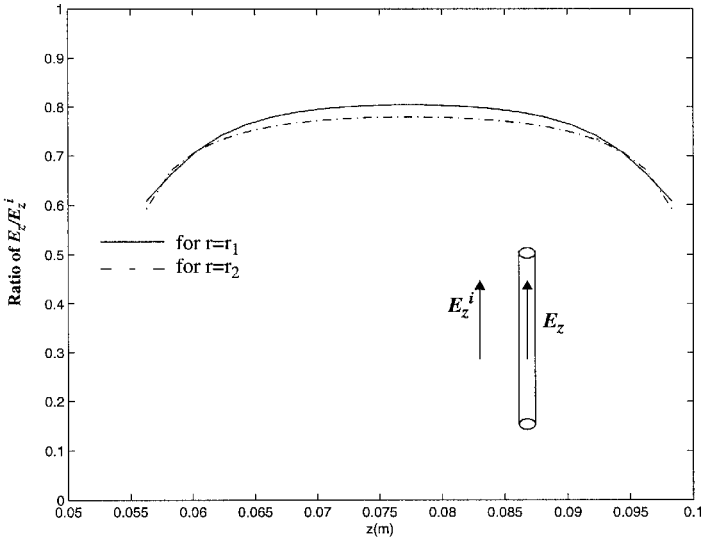
Figure 4. Ratio of E_z/E_z^i varies in the z direction at the different locations of r. The dimensions of the material sample are $d_0 = 0.008\,\text{m}$ and $h_0 = 0.044\,\text{m}$ with the relative permittivity of $\varepsilon = 2.5$. The initial field is assumed to be a TM_{012} mode operating at $2.45\,\text{GHz}$.

Green's function behind the integration sign (see Appendix II), another delta function is needed to be generated from the third term to cancel the second term. Thus, we will need much more summation terms for this special case to meet this requirement. However, if we increase the upper limit in the double summation, the numerical results become closer to the theoretical estimation but at the expense of increasing the computation time.

For this thin dielectric rod material sample, if we employ the scheme of separating the material sample into boundary layer and interior volume regions, the results are improved and at the same time the computation time is reduced. In this computation, the dimensions of the material sample are: $d_0 = 0.008\,\text{m}$ and $h_0 = 0.044\,\text{m}$ with $n_d = 1$ and $l_d = 20$ for the division of the interior volume region. The dimensions of the volume cells in the boundary layer region are: $br = 0.002\,\text{m}$ and $bz = 0.002\,\text{m}$ in the r and z directions, respectively. The number of the total volume cells in the boundary layer and interior volume regions is: $2 \times 22 = 44$ which is the same as the previous

computation. The cavity resonant frequency shift is assumed to be 1% after the material sample is placed inside. The upper limits in the modes summation are chosen as 200 for the boundary layer region and 150 for the interior volume region. The numerical results are shown in Fig. 5.

Since we are only interested in the induced electric field inside the material sample, only the solutions for the volume cells in the interior volume region are plotted in Fig. 5. Because the numerical results show that the z components of the induced electric field dominate in the material sample, only the ratios of the z components of the induced electric fields to that of the initial electric field in the interior volume region are plotted as a function of z in Fig. 5. We observe that the ratios are now very close to 1.

In the scheme of separating the material sample into the boundary layer and interior volume regions for the thin dielectric rod material sample, we keep the number of the volume cells the same as the previous computation. However, the upper limit of the modes summation in the interior volume region is reduced to 150. Hence, the computation time is saved and at the same time better results are obtained.

5.4 Lossy Material Sample

In this numerical example, we will assume that the material sample has a complex relative permittivity of $\varepsilon_r = \varepsilon' - j\varepsilon''$. In this computation, we assume $\varepsilon' = 2.5$ and $\varepsilon'' = 1.5$ with the dimensions of the material sample as: $d_0 = 0.008\,\text{m}$ and $h_0 = 0.008\,\text{m}$. The numerical results are shown in Fig. 6.

In Fig. 6, we plot the ratios of the z components of the induced electric field to that of the initial electric field inside the material sample. Due to the complex permittivity of the material sample, the induced electric field has both the real and imaginary parts. Therefore, in Fig. 6 the upper graphs are for the real part and the lower ones are for the imaginary part of the ratios.

5.5 Inhomogeneous Material Sample

In this numerical example, we assume that the material sample is composed of two kinds of dielectric materials as shown in Fig. 7. The relative permittivities of the two regions of the material sample are denoted as ε_1 and ε_2 and their radii and heights denoted as r_1, r_2
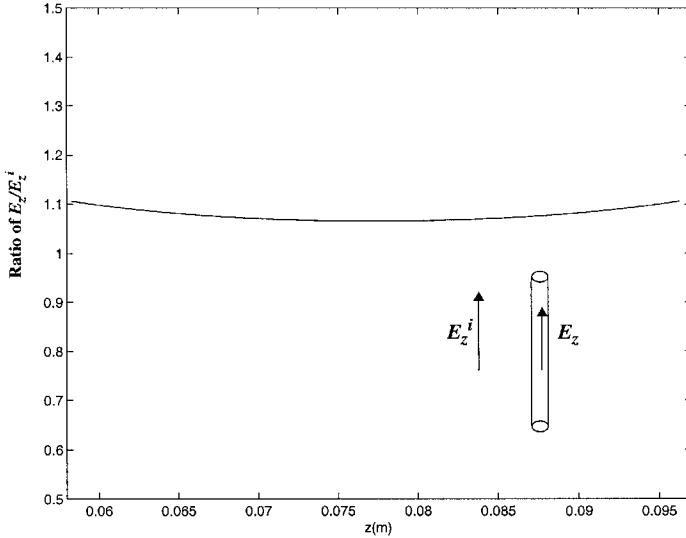
Figure 5. Ratio of E_z/E_z^i varies in the z direction with the scheme of separating the material sample into the boundary layer and interior volume regions. The dimensions of the material sample are $d_0 = 0.008\,\text{m}$ and $h_0 = 0.044\,\text{m}$ with the relative permittivity of $\varepsilon = 2.5$. The initial field is assumed to be a TM_{012} mode operating at $2.45\,\text{GHz}$.

and h_1, h_2, respectively.

If the dimensions of the material sample are electrically small compared with the operating wavelength and the diameter/height ratio is close to one, we can estimate the ratios of the z components of the induced electric fields inside the material sample to that of the initial electric field by the electrostatic approximations of a corresponding concentric sphere with two different dielectric regions as [23],

$$\frac{E_1}{E_0} = \frac{-9\varepsilon_0\varepsilon_2 r_1^{-3}}{(\varepsilon_1 + 2\varepsilon_2)(\varepsilon_2 + 2\varepsilon_0)r_1^{-3} + 2(\varepsilon_1 - \varepsilon_2)(\varepsilon_2 - \varepsilon_0)r_2^{-3}} \quad (33)$$

$$\frac{E_2}{E_0} = 3\varepsilon_0 \frac{(\varepsilon_1 - \varepsilon_2)r^{-3} - (\varepsilon_1 + 2\varepsilon_2)r_1^{-3}}{(\varepsilon_1 + 2\varepsilon_2)(\varepsilon_2 + 2\varepsilon_0)r_1^{-3} + 2(\varepsilon_1 - \varepsilon_2)(\varepsilon_2 - \varepsilon_0)r_2^{-3}} \quad (34)$$

In this numerical example, the dimensions of this inhomogeneous material sample are chosen as: $r_1 = 0.002\,\text{m}$, $h_1 = 0.004\,\text{m}$, $r_2 = 0.004\,\text{m}$ and $h_2 = 0.008\,\text{m}$, and with the relative permittivities as $\varepsilon_1 = 2.5$
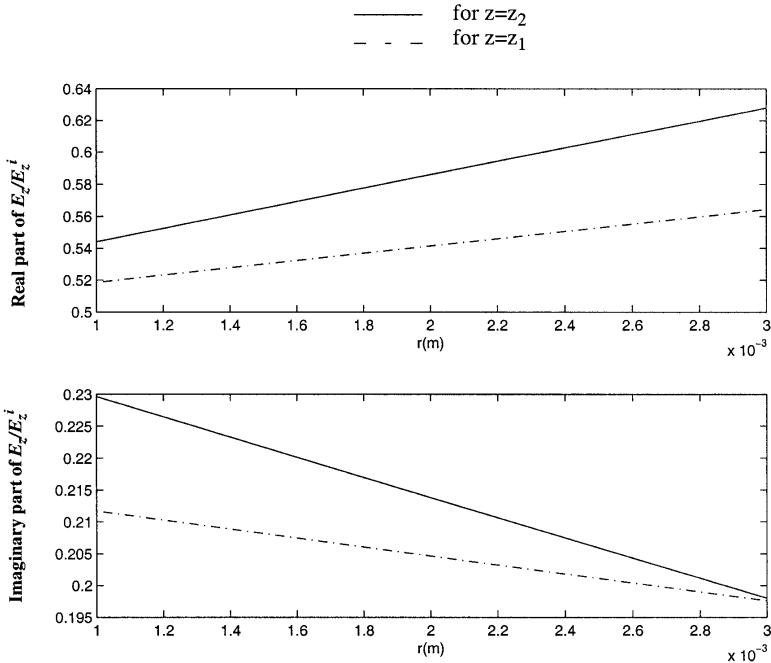
Figure 6. Ratios of E_z/E_z^i varies in the r direction. Each curve represents this ratio as a function of r for different locations of z in a material sample when the material sample has a complex permittivity of $\varepsilon_r = 2.5 - j1.5$. The dimensions of the material sample are: diameter $d_0 = 0.008\,\mathrm{m}$ and height $h_0 = 0.008\,\mathrm{m}$. The upper graphs are for the real part of the ratios and the lower ones are for the imaginary part of the ratios. The initial field is assumed to be a TM_{012} mode operating at $2.45\,\mathrm{GHz}$.

and $\varepsilon_2 = 4.0$. Equations (33) and (34) give the electrostatic estimations of the ratios of the z components of the induced electric fields in the inhomogeneous material sample to that of the initial electric field as 0.5818 in region 1 and 0.5091 in region 2. The numerical results are shown in Fig. 8, where we observe that the numerical results are consistent with the electrostatic estimations.
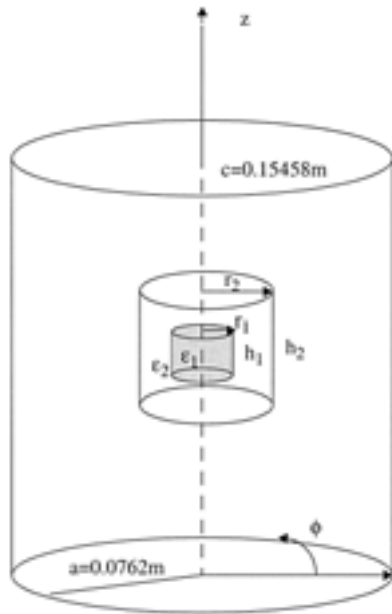
Figure 7. An inhomogeneous material sample is placed in the center of a cylindrical cavity.

5.6 Irregularly Shaped Material Sample

In this numerical example, we assume the material sample to have an irregular shape but keep the material sample azimuthally symmetrical in order to save the computation time. The shape of the material sample is shown in Fig. 9. We assume the dimensions of the material sample as: $h_1 = 0.004\,\text{m}$, $h_2 = 0.008\,\text{m}$, $d_1 = 0.016\,\text{m}$ and $d_2 = 0.008\,\text{m}$, and with the relative permittivity of $\varepsilon_1 = 2.5$. The numerical results are shown in Fig. 10.

5.7 Numerical Convergence

In our numerical calculations, we transformed the triple summation into double summation in order to reduce the computation time. The singularity of the dyadic Green's function, however, still exists. After this transformation the singularity is expressed in the form of k_{gnm} in Eq. (26). We used the resonant frequency shifting to handle the singularity integration problem.
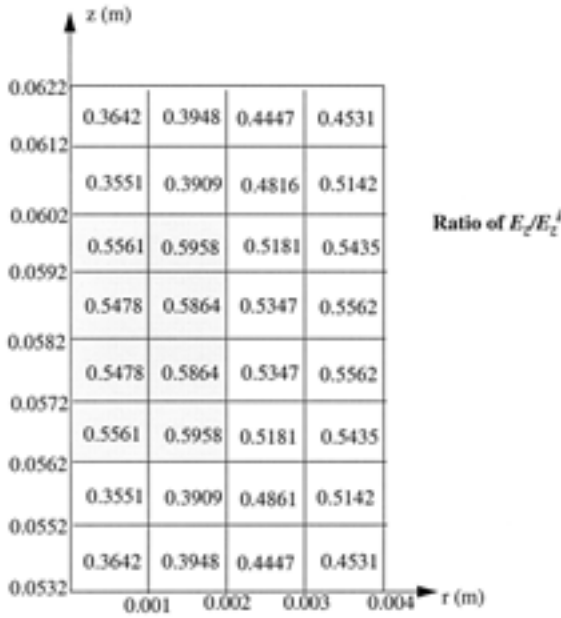
Figure 8. Ratios of E_z/E_z^i in the inhomogeneous material sample with the dimensions of $r_1 = 0.002\,\text{m}$, $h_1 = 0.004\,\text{m}$, $r_2 = 0.004\,\text{m}$ and $h_2 = 0.008\,\text{m}$, where the relative permittivity in the shadowed region is $\varepsilon_1 = 2.5$ and that in the non-shadowed region is $\varepsilon_2 = 4.0$. The electrostatic estimations of the ratios are $R_1 = 0.5818$ and $R_2 \approx 0.5091$. The initial field is assumed to be a TM_{012} mode operating at 2.45 GHz.

In our numerical calculation for various material samples, it was found empirically [23] that we need to sum up $(200)^3$ modes to reach the numerical convergence of the Green's functions for a three-dimensional case. If the symmetry was applied to reduce the problem to a two-dimensional case, only $(200)^2$ modes are needed in the summation. For the discretation of the material sample into volume cells, it was found that as long as the dimension of the volume cells is smaller than 1/10 wavelength, fairly accurate results can be produced.
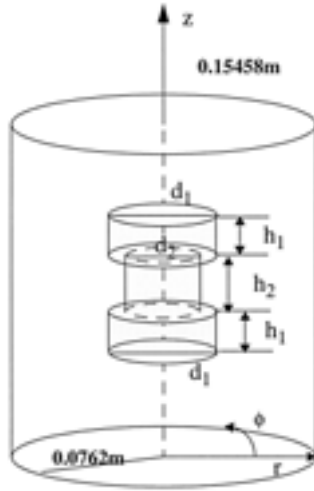
Figure 9. Geometry of an irregularly shaped material sample placed in the cylindrical cavity. The material sample is azimuthally symmetrical and the center of the material sample is consistent with the center of the cylindrical cavity.
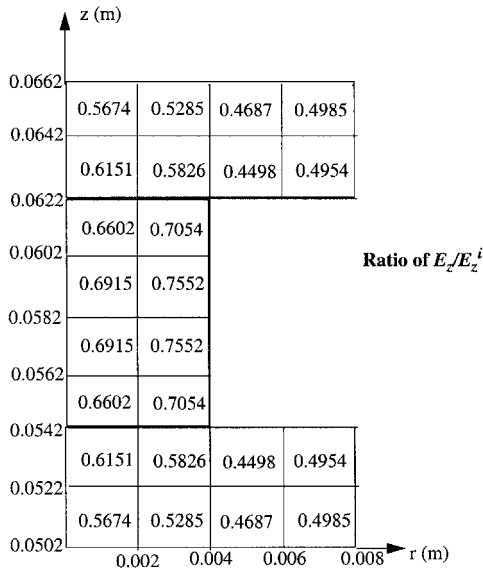

Figure 10. Ratios of E_z/E_z^i in an irregularly shaped material sample. The initial field is assumed to be a TM_{012} mode operating at 2.45 GHz.

6. CONCLUSIONS

In this paper, the integral equation method is applied to quantify the induced electric field in a material sample placed in a cylindrical cavity. Numerical results demonstrate that the integral equation method is a powerful technique. It can be employed to solve the problem involving the material sample with any arbitrary shape or heterogeneity. The only disadvantage of the integral equation method is its slow numerical convergence and a large computation time. To our best knowledge, this is the first attempt to solve this type of problem using the integral equation method.

APPENDIX I: VECTOR WAVE FUNCTIONS, $\vec{L}_{nml}$, $\vec{M}_{nml}$ AND $\vec{N}_{nml}$, IN A CYLINDRICAL CAVITY

The expressions for these vector wave functions are:

$$
\vec{L}_{nml} = \sqrt{\frac{\varepsilon_{0n}\varepsilon_{0l}}{\pi c}} \frac{1}{a J_n'(p_{nm})} \frac{1}{k_{nml}} \left[\hat{r}\frac{p_{nm}}{a} J_n'\left(\frac{p_{nm}}{a}r\right) \cos(n\varphi)\sin\left(\frac{l\pi}{c}z\right) \right.
$$
$$
- \hat{\varphi}\frac{n}{r} J_n\left(\frac{p_{nm}}{a}r\right)\sin(n\varphi)\sin\left(\frac{l\pi}{c}z\right)
$$
$$
\left. + \hat{z}\frac{l\pi}{c} J_n\left(\frac{p_{nm}}{a}r\right)\cos(n\varphi)\cos\left(\frac{l\pi}{c}z\right) \right] \tag{I.1}
$$

$$
\vec{M}_{nml} = \sqrt{\frac{\varepsilon_{0n}\varepsilon_{0l}}{\pi c}} \frac{1}{p_{nm}'\sqrt{1-n^2/p_{nm}'^2}J_n(p_{nm}')} \left[\hat{r}\frac{n}{r} J_n\left(\frac{p_{nm}'}{a}r\right)\cos(n\varphi) \right.
$$
$$
\left. \cdot \sin\left(\frac{l\pi}{c}z\right) - \hat{\varphi}\frac{p_{nm}'}{a} J_n'\left(\frac{p_{nm}'}{a}r\right)\sin(n\varphi)\sin\left(\frac{l\pi}{c}z\right) \right] \tag{I.2}
$$

$$
\vec{N}_{nml} = -\sqrt{\frac{\varepsilon_{0n}\varepsilon_{0l}}{\pi c}} \frac{1}{p_{nm}J_n'(p_{nm})} \frac{1}{k_{nml}} \left[\hat{r}\frac{p_{nm}}{a}\frac{l\pi}{c} J_n'\left(\frac{p_{nm}}{a}r\right)\cos(n\varphi) \right.
$$
$$
\cdot \sin\left(\frac{l\pi}{c}z\right) - \hat{\varphi}\frac{n}{r}\frac{l\pi}{c} J_n\left(\frac{p_{nm}}{a}r\right)\sin(n\varphi)\sin\left(\frac{l\pi}{c}z\right)
$$
$$
\left. + \hat{z}\left(\frac{p_{nm}}{a}\right)^2 J_n\left(\frac{p_{nm}}{a}r\right)\cos(n\varphi)\cos\left(\frac{l\pi}{c}z\right) \right] \tag{I.3}
$$

where ε_{0n} is defined in Eq. (25). Parameters p_{nm} and p_{nm}' are the mth roots of the nth Bessel function $J_n(r)$ and the derivative of the nth Bessel function, $J_n'(r)$, respectively. Dimensions a and c are the radius and height of the cavity, respectively.

The vector wave functions satisfy the following wave equations:

$$\nabla^2 \vec{L}_{nml} + k_{nml}^2 \vec{L}_{nml} = 0, \qquad \nabla \times \vec{L}_{nml} = 0$$

$$\nabla^2 \vec{M}_{nml} + q_{nml}^2 \vec{M}_{nml} = 0, \qquad \nabla \cdot \vec{M}_{nml} = 0$$

$$\nabla^2 \vec{N}_{nml} + k_{nml}^2 \vec{N}_{nml} = 0, \qquad \nabla \cdot \vec{N}_{nml} = 0$$

where $k_{nml}^2 = \left(\frac{p_{nm}}{a}\right)^2 + \left(\frac{l\pi}{c}\right)^2$, $q_{nml}^2 = \left(\frac{p'_{nm}}{a}\right)^2 + \left(\frac{l\pi}{c}\right)^2$.

APPENDIX II: DERIVATION OF EFIE (13)

Substitution of Eq. (7) into Eq. (4) gives

$$\sum_n \left[-k_0^2 a_n \vec{L}_n(\vec{r}) + b_n(q_n^2 - k_0^2)\vec{M}_n(\vec{r}) + c_n(k_n^2 - k_0^2)\vec{N}_n(\vec{r}) \right]$$

$$= -j\omega\mu_0 \vec{J}_{eq}(\vec{r}) \tag{II.1}$$

based on the properties of $\vec{L}_n$, $\vec{M}_n$, and $\vec{N}_n$ functions as given in Appendix I.

Due to the orthogonality of $\vec{L}_n$, $\vec{M}_n$, and $\vec{N}_n$ functions, a_n, b_n, and c_n can be determined from Eq. (II.1) as

$$a_n = \frac{j\omega\mu_0}{k_0^2} \int_{v_{\text{sample}}} \vec{J}_{eq}\left(\vec{r}'\right) \cdot \vec{L}_n\left(\vec{r}'\right) dv'$$

$$(\text{because } J_{eq}\left(\vec{r}'\right) \text{ exists only in } v_{\text{sample}})$$

$$b_n = \frac{-j\omega\mu_0}{q_n^2 - k_0^2} \int_{v_{\text{sample}}} \vec{J}_{eq}\left(\vec{r}'\right) \cdot \vec{M}_n\left(\vec{r}'\right) dv'$$

$$c_n = \frac{-j\omega\mu_0}{k_n^2 - k_0^2} \int_{v_{\text{sample}}} \vec{J}_{eq}\left(\vec{r}'\right) \cdot \vec{N}_n\left(\vec{r}'\right) dv'$$

Therefore,

$$\vec{E}^s(\vec{r}) = -j\omega\mu_0 \int_{v_{\text{sample}}} \vec{J}_{eq}(\vec{r}') \cdot \overline{G}_e(\vec{r}', \vec{r}) \, dv' \tag{II.2}$$

where

$$\overline{G}_e\left(\vec{r}', \vec{r}\right) = \sum_n \left[\frac{-\vec{L}_n(\vec{r}')\vec{L}_n(\vec{r})}{k_0^2} + \frac{\vec{M}_n(\vec{r}')\vec{M}_n(\vec{r})}{q_n^2 - k_0^2} + \frac{\vec{N}_n(\vec{r}')\vec{N}_n(\vec{r})}{k_n^2 - k_0^2} \right] \tag{II.3}$$

$$q_n^2 = \left(\frac{p'_{nm}}{a}\right)^2 + \left(\frac{l\pi}{c}\right)^2$$

$$k_n^2 = \left(\frac{p_{nm}}{a}\right)^2 + \left(\frac{l\pi}{c}\right)^2 \qquad k_0^2 = \omega^2 \mu_0 \varepsilon_0$$

$$p'_{nm} = \text{the } m\text{th root of } J'_n(x) = 0$$

$$p_{nm} = \text{the } m\text{th root of } J_n(x) = 0$$

If the identity [24] of

$$\sum_n \left[\vec{L}_n(\vec{r}')\vec{L}_n(\vec{r}) + \vec{M}_n(\vec{r}')\vec{M}_n(\vec{r}) + \vec{N}_n(\vec{r}')\vec{N}_n(\vec{r}) \right] = \overline{I}\delta\left(\vec{r} - \vec{r}'\right) \quad \text{(II.4)}$$

is used, we can rewrite

$$\overline{G}_e = \overline{G}_{e0} - \frac{\overline{I}}{k_0^2}\delta\left(\vec{r} - \vec{r}'\right) \tag{II.5}$$

where

$$\overline{G}_{e0} = \sum_n \left[\frac{q_n^2 \vec{M}_n(\vec{r}')\vec{M}_n(\vec{r})}{k_0^2(q_n^2 - k_0^2)} + \frac{k_n^2 \vec{N}_n(\vec{r}')\vec{N}_n(\vec{r})}{k_0^2(k_n^2 - k_0^2)} \right] \tag{II.6}$$

If Eq. (II.5) is substituted into Eq. (II.2), we have

$$\vec{E}^s(\vec{r}) = \frac{j\omega\mu_0}{k_0^2}\vec{J}_{eq}(\vec{r}) - j\omega\mu_0 \int\limits_{v_{\text{sample}}} \vec{J}_{eq}\left(\vec{r}'\right) \cdot \overline{G}_{e0}\left(\vec{r}',\vec{r}\right) dv'$$

$$= \frac{j\omega\mu_0\tau_e}{k_0^2}\vec{E}(\vec{r}) - j\omega\mu_0 \int\limits_{v_{\text{sample}}} \tau_e\left(\vec{r}'\right)\vec{E}\left(\vec{r}'\right) \cdot \overline{G}_{e0}\left(\vec{r}',\vec{r}\right) dv' \quad \text{(II.7)}$$

Substituting Eq. (II.7) into the relation of $\vec{E}(\vec{r}) = \vec{E}^s(\vec{r}) + \vec{E}^i(\vec{r})$, we obtain the EFIE:

$$\vec{E}(\vec{r})\left(1 - \frac{j\omega\mu_0\tau_e(\vec{r})}{k_0^2}\right) + j\omega\mu_0 \int\limits_{v_{\text{sample}}} \tau_e\left(\vec{r}'\right)\vec{E}\left(\vec{r}'\right) \cdot \overline{G}_{e0}\left(\vec{r}',\vec{r}\right) dv' = \vec{E}^i(\vec{r})$$

$$\text{(II.8)}$$

As we know, there exists very poor convergence property in the dyadic Green's function G_e [24]. However, extracting the delta function from the dyadic Green's function G_e does not improve its singularity or

convergency. Our main purpose is to make EFIE (13) and MFIE (14) consistent. Therefore, we may only solve EFIE (13) in our numerical computations.

ACKNOWLEDGMENT

REFERENCES

1. Zaki, K. A., and A. E. Atia, "Modes in dielectric-loaded waveguides and resonators," *IEEE Trans. on Microwave Theory and Technologies*, Vol. MTT-31, No. 12, 1039–1045, Dec. 1983.

2. Kajbez, D., A. V. Glisson, and J. James, "Computed modal field distribution for isolated dielectric resonators," *1984 IEEE MTT-S International Microwave Symposium Digest*, 193–195, June 1984.

3. Zaki, K. A., and C. Chen, "Intensity and distribution of hybrid-mode fields in dielectric-loaded waveguides," *IEEE Trans. on Microwave Theory and Technologies*, Vol. MTT-33, No. 12, 1442–1447, Dec. 1985.

4. Maj, S., and M. Pospieszalski, "A composite cylindrical dielectric resonator," *1984 IEEE MTT-S International Microwave Symposium Digest*, 190–192, June 1984.

5. Krupka, J., "Optimization of an electromagnetic basis for determination of the resonant frequency of microwave cavities partially filled with a dielectric," *IEEE Trans. on Microwave Theory and Technologies*, Vol. MTT-31, No. 3, 302–305, March 1983.

6. Kajfez, D., A. V. Glisson, and J. James, "Computed modal field distribution for isolated dielectric resonators," *IEEE Trans. on Microwave Theory and Technologies*, Vol. MTT-32, No. 12, 1609–1616, Dec. 1984.

7. Ayappa, K. G., H. T. Davis, E. A. Davis, and J. Gordon, "Two-dimensional finite element analysis of microwave heating," *AIChE Journal*, Vol. 38, 1577–1592, Oct. 1992.

8. Jia, X., and P. Jolly, "Simulation of microwave field and power distribution in a cavity by a three-dimensional finite element method," *Journal of Microwave Power and Electromagnetic Energy*, Vol. 27, No. 1, 11–22, 1992.

9. Liu, F., I. Turner, and M. Bialkowski, "A finite-difference time-domain simulation of power density distribution in a dielectric loaded microwave cavity," *Journal of Microwave Power and Electromagnetic Energy*, Vol. 29, 138–148, 1994.

10. Zhao, H., I. Turner, and F. W. Liu, "Numerical simulation of the power density distribution generated in a multimode cavity by using the method of lines technique to solve directly for the electric field," *IEEE Trans. on Microwave Theory and Technologies*, Vol. MTT-44, 2185–2194, 1996.

11. Torres, F., and B. Jecko, "Complete FDTD analysis of microwave heating processing in frequency-dependent and temperature-dependent media," *IEEE Trans. Microwave Theory Tech.*, Vol. MTT-45, 108–117, 1997.

12. Fu, W., and A. Metaxas, "Numerical prediction of three-dimensional power density distribution in a multi-mode cavity," *Journal of Microwave Power and Electromagnetic Energy*, Vol. 29, 67–75, 1994.

13. Tai, C. T., *Dyadic Green's Functions in Electromagnetic Theory*, second edition, IEEE Press, 1993.

14. Johnson, W. A., A. Q. Howard, and D. G. Dudley, "On the irrotational component of the electric Green's function," *Radio Science*, Vol. 14, 961–967, 1979.

15. Collin, R. E., "On the incompleteness of E and H modes in waveguides," *Can. J. Phys.*, Vol. 51, 1135–1140, 1973.

16. Howard, A. Q., "On the longitudinal component of the Green's function dyadic," *Proc. IEEE*, Vol. 62, 1704–1705, 1974.

17. Tai, C. T., "Equivalent layers of surface charge, current sheet, and polarization in the eigenfunction expansions of Green's functions in electromagnetic theory," *IEEE Trans. Antennas and Propagation*, Vol. AP-20, 733–739, 1981.

18. Tai, C. T., and P. Rozenfeld, "Different representations of dyadic Green's functions for a rectangular cavity," *IEEE Trans. Microwave Theory Tech.*, Vol. MTT-24, 597–601, 1976.

19. Zhang, J., and K. M. Chen, "Mode-matching analysis of the induced electric field in a material sample placed within an energized cylindrical cavity," current issue.

20. Hansen, W. W., "A new type of expansion in radiation problems," *Physics Review*, Vol. 47, 139–143, 1935.

21. Hansen, W. W., "Directional characteristic of antenna over a plane earth," *Journal of Applied Physics*, Vol. 7, 460–465, 1936.

22. Hansen, W. W., "Transformations useful in certain antenna calculation," *Journal of Applied Physics*, Vol. 8, 282–286, 1937.

23. Zhang, J., "Interaction of electromagnetic fields with a material sample placed within an energized cavity," Ph.D. Dissertation, Michigan State University, 1998.
24. Collin, R. E., *Field Theory of Guided Waves*, second edition, IEEE Press, 1991.
25. Stratton, J. A., *Electromagnetic Theory*, McGraw-Hill Book Company, Inc., New York, NY, 1941.
26. Tai, C. T., "On the eigenfunction expansion of dyadic Green's functions," *Proc. IEEE*, Vol. 61, 480–481, Apr. 1973.
27. Harrington, R. F., *Time-Harmonic Electromagnetic Fields*, McGraw-Hill, New York, 1961.